JOURNAL OF COMPUTATIONAL PHYSICS 121, 102–114 (1995)

Decomposition and Inversion of Elastic Reflection Data; First-Order Angular Dependence and Applications

ALVIN K. BENSON

Brigham Young University, Department of Geology and Geophysics, 359C ESC, Provo, Utah 84602

Received May 16, 1994; revised February 23, 1995

The elastic wave displacement equation is transformed into pressure–stress coordinates, where the Born approximation of the Lippman-Schwinger equation in the Fourier-transform domain is employed to decompose the observed fields into their scattered components: *P-P*, *P-S*, *S-P*, and *S-S*. Triple Fourier transforms of the scattered elastic wave data are linear combinations of the double Fourier transforms of the relative changes in the medium properties. Angular-dependent reflection coefficients for each of the scattering modes are constructed, and an inversion algorithm is outlined. Inversion of the observed elastic wave fields is accomplished in a manner similar to the acoustic problem. Density, bulk modulus, and shear modulus variations in an elastic earth can be recovered by utilizing the angular-dependent information present in the observed wave fields. Examples illustrate these points. Transforming the elastic wave data back to displacement coordinates and assuming a compressional source, an analysis of recorded amplitudes yields some practical answers about converted-wave data. Significant amounts of $P \rightarrow S$ data should typically be generated by compressional sources, with significant contributions at smaller angles. However, signal-to-noise calculations suggest that more sweeps and more geophone channels at longer offsets will typically be necessary to get *P-S* sections of comparable quality to *P-P* sections.

INTRODUCTION

Seismic inversion algorithms range from traveltime inversion [5, 14, 7, 1, 11, 9, 13, and many others] to Born inversion [4, 21, 10, 2, 3, 22, and others] to full-wave inversion [8, 18, and others]. Traveltime inversion typically uses ray tracing to compute both the traveltimes and the perturbations of traveltimes with respect to velocity. Although computationally efficient, traveltime inversion can fail when the earth's velocity variations are characterized by the same wavelength as in the source wavelet. However, a conjugate gradient optimization algorithm can sometimes determine a correct velocity model fairly quickly, and successful inversion can result even when the starting model is far from the actual model.

Full-wave inversion overcomes limitations imposed by the high-frequency restrictions in traveltime inversion and the weak scattering approximation of Born methods by perturbing the velocity model until the synthetic seismograms match the observed seismograms. The synthetic seismograms are usually computed by a finite-difference solution to the wave equation, and few approximations are necessary. However, the procedure can fail because the normed difference between the observed and synthetic seismograms can be highly nonlinear with respect to the velocity models.

To bridge the gap between the extremes of traveltime and full-wave inversion, linearized Born inversion and other amplitude methods have been employed. These intermediate methods can be highly successful for some data sets, but not typically for data with strong impedance contrasts. Other intermediate methods include surface-wave inversion [20] and diffraction tomography [12]. This paper will concentrate on linearized decomposition and inversion of seismic data using the elastic wave equation.

ELASTIC WAVE EQUATION

Clayton and Stolt [4] applied the Born approximation to the acoustic wave equation and related the reflectivity function to variations in the density and bulk modulus of the medium. A similar approach is implemented in this paper for the elastic wave equation, leading to four reflectivity functions that depend on variations in three medium parameters—the density, the bulk modulus, and the shear modulus. The beginning point of this particular derivation is the two-dimensional elastic displacement equation [6], which is written here in matrix form,

$$LU = \left[\rho\omega^2 \begin{pmatrix} 1 & 0 \\ 0 & 1 \end{pmatrix} + \begin{pmatrix} \partial_x K\partial_x + \partial_z \mu \partial_z & \partial_x(K-2\mu)\partial_z + \partial_z \mu \partial_x \\ \partial_z(K-2\mu)\partial_x + \partial_x \mu \partial_z & \partial_x \mu \partial_x + \partial_z K \partial_z \end{pmatrix}\right] \times \begin{bmatrix} U_x \\ U_z \end{bmatrix} = 0, \tag{1}$$

where U = displacement,
ρ = density,
K = bulk modulus,

0021-9991/95 $12.00

μ = shear modulus,
ω = frequency.

The spatial and temporal dependence of operators, such as L, will be suppressed until later.

If the density, bulk modulus, and shear modulus are all constant background values, i.e., $\rho = \rho_r$, $K = K_r$, and $\mu = \mu_r$, then the operator L in Eq. (1) becomes

$$L_r = \left[\rho\omega^2 \begin{pmatrix} 1 & 0 \\ 0 & 1 \end{pmatrix} + \begin{pmatrix} K_r\partial_x^2 + \mu_r\partial_z^2 & (K_r - \mu_r)\partial_x\partial_z \\ (K_r - \mu_r)\partial_x\partial_z & \mu_r\partial_x^2 + K_r\partial_z^2 \end{pmatrix}\right]. \quad (2)$$

It is convenient to rewrite L_r in diagonalized form by using the operator

$$H = \begin{pmatrix} \partial_x & \partial_z \\ -\partial_z & \partial_x \end{pmatrix}. \quad (3)$$

Then

$$L_r = H^{-1} \begin{pmatrix} K_r L_P & 0 \\ 0 & \mu_r L_S \end{pmatrix} H, \quad (4)$$

where

$$L_P = (\rho\omega^2/K_r) + \nabla^2, \quad (5a)$$

$$L_S = (\rho\omega^2/\mu_r) + \nabla^2, \quad (5b)$$

and H^{-1} is the inverse operator of H.

The Green's operator associated with the wave operator L_r is formally defined as [19, p. 129]

$$G_r \equiv -L_r^{-1}. \quad (6)$$

Likewise, if we define $G_P \equiv -L_P^{-1}$ and $G_S \equiv -L_S^{-1}$, then

$$G_r = H^{-1} \begin{pmatrix} G_P/K_r & 0 \\ 0 & G_S/\mu_r \end{pmatrix} H. \quad (7)$$

The latter equation can be rewritten as

$$\begin{pmatrix} G_P & 0 \\ 0 & G_S \end{pmatrix} = \begin{pmatrix} K_r & 0 \\ 0 & \mu_r \end{pmatrix} HG_rH^{-1}, \quad (8)$$

which expresses G_r in the pressure–stress (P-S) coordinate system (vs displacement coordinates).

THE SCATTERING EQUATIONS—BORN APPROXIMATION

To relate G (the Green's operator for L in Eq. (1)) and G_r, we will employ the simple identity

$$A = B + B(B^{-1} - A^{-1})A$$

and associate G with A and G_r with B. Consequently, if we define $V = L - L_r$, then

$$G = G_r + G_rVG, \quad (9)$$

which is the Lippmann–Schwinger equation for G, and V corresponds to the scattering potential. Equation (9) is valid for any choice of G_r that satisfies the same external boundary conditions as G. Formally solving Eq. (9) for G,

$$G = (1 - G_rV)^{-1}G_r. \quad (10)$$

Keeping the first two terms of the Born series expansion of Eq. (10) yields the Born approximation to the Lippmann–Schwinger equation:

$$G \approx G_r + G_rVG_r. \quad (11)$$

If L_r is close enough to L that G_r reasonably models the direct wave between the source and receiver, then G_rVG_r should model simple reflections, and the discarded higher terms should involve multiple reflections only.

For elastic waves, the scattering potential V is the difference between the wave operators L (Eq. 1) and L_r (Eq. 2),

$$V = L - L_r = \left[\rho_r a_1\omega^2 \begin{pmatrix} 1 & 0 \\ 0 & 1 \end{pmatrix} + \begin{pmatrix} K_r\partial_x a_2\partial_x + \mu_r\partial_z a_3\partial_z & K_r\partial_x a_2\partial_z + \mu_r(\partial_z a_3\partial_x - 2\partial_x a_3\partial_z) \\ K_r\partial_z a_2\partial_x + \mu_r(\partial_x a_3\partial_z - 2\partial_z a_3\partial_x) & \mu_r\partial_x a_3\partial_x + K_r\partial_z a_2\partial_z \end{pmatrix}\right], \quad (12)$$

where

$$a_1 = [(\rho/\rho_r) - 1], \quad (13a)$$

$$a_2 = [(K/K_r) - 1], \quad (13b)$$

$$a_3 = [(\mu/\mu_r) - 1], \quad (13c)$$

and a_1 represents the variations in density, a_2 represents the spatial variations in bulk modulus relative to the reference bulk modulus, and a_3 represents the variations in shear modulus relative to the reference shear modulus. Note that these perturbation parameters a_i are defined slightly differently in this paper than in Clayton and Stolt [4] and Stolt and Weglein [16].

It is convenient to define the data scattered wave field D as the impulse response G minus the direct wave arrival G_r [4]. Using Eq. (7) and the Born approximation in Eq. (11), the relationship between the data field and the scattering potential is

$$\begin{aligned} D &= (G - G_r)S(\omega) = G_r V G_r S(\omega) \\ &= H^{-1}\begin{pmatrix} G_P/K_r & 0 \\ 0 & G_S/\mu_r \end{pmatrix} HVH^{-1}\begin{pmatrix} G_P/K_r & 0 \\ 0 & G_S/\mu_r \end{pmatrix} HS(\omega), \end{aligned} \tag{14}$$

where $S(\omega)$ is the Fourier transform of the source time function.

ELASTIC WAVE COMPONENTS OF REFLECTIVITY

If the source generates both compressional and shear waves, then the observed data field would generally consist of four types of scattered waves: (a) $P \rightarrow P$ primary scattering (D_{PP}); (b) $S \rightarrow P$ converted scattering (D_{SP}); (c) $P \rightarrow S$ converted scattering (D_{PS}); and (d) $S \rightarrow S$ primary scattering (D_{SS}). Performing the same transformation on the data as was applied to the Green's functions (Eq. (8)), and using Eqs. (3), (4), (12), and (14), the data can be represented in the pressure–stress (P-S) domain as

$$\begin{aligned} &\begin{pmatrix} D_{PP} & D_{SP} \\ D_{PS} & D_{SS} \end{pmatrix} \\ &= \begin{pmatrix} K_r & 0 \\ 0 & \mu_r \end{pmatrix} HDH^{-1}S(\omega) \\ &= \begin{pmatrix} G_P & 0 \\ 0 & G_S \end{pmatrix} HVH^{-1}\begin{pmatrix} G_P/K_r & 0 \\ 0 & G_S/\mu_r \end{pmatrix} S(\omega) \qquad (15) \\ &= \begin{pmatrix} G_P & 0 \\ 0 & G_S \end{pmatrix}\left[\begin{pmatrix} K_r a_2 & 0 \\ 0 & \mu_r a_3 \end{pmatrix}\nabla^2 \right. \\ &\quad \left. + H\begin{pmatrix} \omega^2 a_1 \rho_r & 2\mu_r(\partial_z a_3 \partial_x - \partial_x a_3 \partial_z)) \\ 2\mu_r(\partial_x a_3 \partial_z - \partial_z a_3 \partial_x) & \omega^2 a_1 \rho_r \end{pmatrix} H^{-1}\right] \\ &\quad \times \begin{pmatrix} G_P/K_r & 0 \\ 0 & G_S/\mu_r \end{pmatrix} S(\omega). \qquad (16) \end{aligned}$$

Since in the space–frequency domain there is an implied convolutional integral over space at every matrix multiplication, Eq. (16) is actually an integral equation [4]. In addition, since most of the operators are differential operators, most of the integrals are simple, but at least one spatial integral will remain.

In the following, we will take the earth to be two-dimensional (2D), although relatively straightforward extensions can be made to 3D (see [4, 17]). In the 2D problem, the recorded data D is a function of the receiver location x_g, z_g the source location x_s, z_s and the frequency. Because the convolution over the spatial variable x becomes a simple multiplication in the Fourier domain, and the derivatives with respect to x become constants ik_x, the simplest expression of Eq. (16) is in the (k_x, z, ω) domain. Using WKBJ Green's operators and notation similar to Clayton and Stolt [4], Eq. (16) becomes

$$\begin{aligned} &\begin{pmatrix} D_{PP}(k_g, z_g | k_s, z_s; \omega) & D_{SP}(k_g, z_g | k_s, z_s; \omega) \\ D_{PS}(k_g, z_g | k_s, z_s; \omega) & D_{SS}(k_g, z_g | k_s, z_s; \omega) \end{pmatrix} \\ &= -(1/4)\int dz \begin{pmatrix} (e^{i\nu_g|z-z_g|})/\nu_g & 0 \\ 0 & (e^{i\eta_g|z-z_g|})/\eta_g \end{pmatrix} \\ &\quad \times \left[\begin{pmatrix} K_r a_2 & 0 \\ 0 & \mu_r a_3 \end{pmatrix}(\partial_z^2 - k_s^2) \right. \qquad (17) \\ &\quad \left. + H\begin{pmatrix} \omega^2 a_1 \rho_r & 2i\mu_r(\partial_z a_3 k_s - k_g a_3 \partial_z) \\ 2i\mu_r(k_g a_3 \partial_z - \partial_z a_3 k_s) & \omega^2 a_1 \rho_r \end{pmatrix} H^{-1}\right] \\ &\quad \times \begin{pmatrix} (e^{i\nu_s|z-z_s|})/(k_r \nu_s) & 0 \\ 0 & (e^{i\eta_s|z-z_s|})/(\mu_r \eta_s) \end{pmatrix} S(\omega), \end{aligned}$$

where k_g and k_s are the wavenumbers corresponding to the Fourier transforms of x_g and x_s, respectively, and

$$\nu_g = (\omega/\alpha_r)\sqrt{1 - (k_g^2\alpha_r^2/\omega^2)}, \tag{18a}$$

$$\eta_g = (\omega/\beta_r)\sqrt{1 - (k_g^2\beta_r^2/\omega^2)}, \tag{18b}$$

$$\nu_s = (\omega/\alpha_r)\sqrt{1 - (k_s^2\alpha_r^2/\omega^2)}, \tag{18c}$$

$$\eta_s = (\omega/\beta_r)\sqrt{1 - (k_s^2\beta_r^2/\omega^2)}, \tag{18d}$$

and

$$\alpha_r^2 = (K_r/\rho_r), \tag{19a}$$

$$\beta_r^2 = (\mu_r/\rho_r). \tag{19b}$$

As can be seen from Eq. (19a), α_r is the reference (background) compressional wave velocity, and from (19b), β_r is the reference (background) shear wave velocity.

Let us consider the case for surface reflection data. The observations of the wave field response are made on the horizontal surface ($z_s = z_g = 0$). We will not consider the presence of a free surface, and so we will stop the medium above the datum from scattering by assuming that $a_1(x, z) = a_2(x, z) = a_3(x, z) = 0$ for $z < 0$. Under these conditions, the absolute value signs in the exponentials in Eq. (17) disappear and the evaluation of the derivatives is simplified. Applying the derivatives to the left of a_1, a_2, and a_3 to the exponentials on their left through integration by parts, we obtain the following expressions for the elastic wave components:

$$D_{PP}(k_g, k_s, \omega) = \int dz\, (e^{i(\nu_g+\nu_s)z}/(4\nu_g\nu_s)) \times [a_2(\omega/\alpha_2)^2 + a_1(\nu_g\nu_s - k_gk_s) - 2a_3(\beta_r/\omega)^2(k_g\nu_s + \nu_gk_s)^2]S(\omega), \quad (20)$$

$$D_{PS}(k_g, k_s, \omega) = -\int dz\, \beta_r^2(e^{i(\eta_g+\nu_s)z}/(4\alpha_r^2\eta_g\nu_s)) \times [a_1(\eta_gk_s + k_g\nu_s) + 2a_3(\beta_r/\omega)^2 \times (\eta_g\nu_s - k_gk_s)(\eta_gk_s + k_g\nu_s)]S(\omega), \quad (21)$$

$$D_{SP}(k_g, k_s, \omega) = \int dz\, \alpha_r^2(e^{i(\nu_g+\eta_s)z}/(4\beta_r^2\nu_g\eta_s)) \times [a_1(k_g\eta_s + \nu_gk_s) + 2a_3(\beta_r/\omega)^2 \times (\nu_g\eta_s - k_gk_s)(k_g\eta_s + \nu_gk_s)]S(\omega), \quad (22)$$

$$D_{SS}(k_g, k_s, \omega) = \int dz\, (e^{i(\eta_g+\eta_s)z}/(4\eta_g\eta_s)) \times [a_1(\eta_g\eta_s - k_gk_s) + a_3((\omega/\beta_r)^2 - 2(\beta_r/\omega)^2(k_g\eta_s + \eta_gk_s)^2)]S(\omega). \quad (23)$$

Strictly speaking, the expressions in Eqs. (20) through (23) are only valid at a particular frequency ω for k_g and k_s sufficiently small in magnitude that the arguments of all the square roots in ν_g, η_g, ν_s, and η_s (Eqs. (18a) through (18d)) are positive. If one or more of these square roots are negative, we are in the evanescent region, and Eq. (17) is still valid as long as proper care of the signs is taken [17]. In the limit of small a_1, a_2, and a_3, the expressions in Eqs. (20)–(23) become exact, and

$$a_1 \approx \ln(\rho/\rho_r), \quad a_2 \approx \ln(K/K_r), \quad a_3 \approx \ln(\mu/\mu_r). \quad (24)$$

Apart from the exponentials, the only z-dependence in the integrals in Eqs. (20) through (23) is the perturbation parameters a_1, a_2, and a_3. Consequently, these four integrals can be represented as linear combinations of Fourier transforms of a_1, a_2, and a_3. Letting $\overline{a_i}(k_x, k_z)$ represent the double Fourier transform of $a_i(x, z)$, Eqs. (20)–(23) become

$$D_{PP}(k_g, k_s, \omega) = (1/4\nu_g\nu_s)[(\omega/\alpha_r)^2\overline{a_2}(k_g - k_s, \nu_g + \nu_s) + (\nu_g\nu_s - k_gk_s)\overline{a_1}(k_g - k_s, \nu_g + \nu_s) - 2(\beta_r/\omega)^2(k_g\nu_s + \nu_gk_s)^2 \times \overline{a_3}(k_g - k_s, \nu_g + \nu_s)]S(\omega), \quad (25)$$

$$D_{PS}(k_g, k_s, \omega) = (-1/4\eta_g\nu_s)(\beta_r/\alpha_r)^2(\eta_g\nu_s + k_g\nu_s) \times [\overline{a_1}(k_g - k_s, \eta_g + \nu_s) + 2(\beta_r/\omega)^2 \times (\eta_g\nu_s - k_gk_s)\overline{a_3}(k_g - k_s, \eta_g + \nu_s)]S(\omega), \quad (26)$$

$$D_{SP}(k_g, k_s, \omega) = (1/4\nu_g\eta_s)(\alpha_r/\beta_r)^2(\nu_gk_s + k_g\nu_s) \times [\overline{a_1}(k_g - k_s, \nu_g + \eta_s) + 2(\beta_r/\omega)^2 \times (\nu_g\eta_s - k_gk_s)\overline{a_3}(k_g - k_s, \nu_g + \eta_s)]S(\omega), \quad (27)$$

$$D_{SS}(k_g, k_s, \omega) = (1/4\eta_g\eta_s)[(\eta_g\eta_s - k_gk_s)\overline{a_1}(k_g - k_s, \eta_g + \eta_s) + ((\omega/\beta_r)^2 - 2(\beta_r/\omega)^2)(k_g\eta_s + \eta_gk_s)^2) \times \overline{a_3}(k_g - k_s, \eta_g + \eta_s)]S(\omega). \quad (28)$$

The P-P reflections (Eq. (25)) respond to changes in all three medium parameters, and the shear modulus contribution to this mode is negative, corresponding to the loss of energy due to mode conversion to P-S waves. On the other hand, the converted-wave data (P-S and S-P) and the S-S data respond to changes in shear modulus and density, but not to changes in bulk modulus.

LINEARIZED INVERSION

To invert Eqs. (25)–(28), the first step is to deconvolve the source $S(\omega)$, and thus define

$$D'(k_g, k_s, \omega) = D(k_g, k_s, \omega)/S(\omega). \quad (29)$$

As pointed out by Clayton and Stolt [4], to avoid instabilities due to $S(\omega)$ being band-limited, we simply set D' to zero outside the frequency band width of $S(\omega)$. This means we will only be able to resolve the variations in a_1, a_2, and a_3 within this passband. The inverse problem for Eqs. (25)–(28) then becomes

$$D'(k_g, k_s, \omega) = \sum_{i=1}^{3} A_i(k_g, k_s, \omega)\overline{a_i}(k_g - k_s, k_z), \quad (30)$$

where

$$k_z = \nu_g + \nu_s, \quad (31a)$$

$$A_1 = (1/4\nu_g\nu_s)(\nu_g\nu_s - k_gk_s), \quad (31b)$$

$$A_2 = (1/4\nu_g\nu_s)(\omega/\alpha_r)^2, \quad (31c)$$

$$A_3 = (-1/2\nu_g\nu_s)(\beta_r/\omega)^2(k_g\nu_s + \nu_gk_s) \quad (31d)$$

for Eq. (25);

$$k_z = \eta_g + \nu_s, \quad (32a)$$

$$A_1 = (-1/4\eta_g\nu_s)(\beta_r/\alpha_r)^2(\eta_gk_s + k_g\nu_s), \quad (32b)$$

$$A_2 = 0, \quad (32c)$$

$$A_3 = (-1/2\eta_g\nu_s)(\beta_r/\omega)^2(\beta_r/\alpha_r)^2(\eta_gk_s + k_g\nu_s)(\eta_g\nu_s - k_gk_s) \quad (32d)$$

for Eq. (26);

$$k_z = \nu_g + \eta_s, \quad (33a)$$

$$A_1 = (1/4\nu_g\eta_s)(\alpha_r/\beta_r)^2(\nu_gk_s + k_g\eta_s), \quad (33b)$$

$$A_2 = 0, \tag{33c}$$

$$A_3 = (1/2\nu_g\eta_s)(\alpha_r/\omega)^2(\nu_g k_s + k_g\eta_s)(\nu_g\eta_s - k_g k_s) \tag{33d}$$

for Eq. (27);

$$k_z = \eta_g + \eta_s, \tag{34a}$$

$$A_1 = (1/4\eta_g\eta_s)(\eta_g\nu_s - k_g k_s), \tag{34b}$$

$$A_2 = 0, \tag{34c}$$

$$A_3 = (1/4\eta_g\eta_s)[(\omega/\beta_r)^2 - 2(\beta_r/\omega)^2](k_g\eta_s + \eta_g k_s)^2 \tag{34d}$$

for Eq. (28).

The slight differences between the A_i for P-P scattering in Eqs. (31b)–(31d) and those of Stolt and Weglein [16] are due to the slightly different definition of our a_i (Eqs. (13a)–(13c)) and that we are presently in pressure–stress coordinates versus displacement coordinates. Equations for the other modes of scattering are not discussed by Stolt and Weglein [16]. From Eq. (30), the a_i can be reconstructed as weighted averages of $D'(k_g, k_s, \omega)$ determined at different offsets by using a least-squares formulation similar to that described by Clayton and Stolt [4].

ANGULAR-DEPENDENT REFLECTION COEFFICIENTS

The coefficients in Eqs. (25) through (28) can be cast in a more physically understandable form by defining the following angles:

$$k_g = (\omega/\alpha_r)\sin(\phi_{Pg}) = (\omega/\beta_r)\sin(\phi_{Sg}), \tag{35a}$$

and

$$k_s = (\omega/\alpha_r)\sin(\phi_{Ps}) = (\omega/\beta_r)\sin(\phi_{Ss}). \tag{35b}$$

Then, the expressions for ν_g, η_g, ν_s, and η_s in Eqs. (18a)–(18d) become

$$\nu_g = (\omega/\alpha_r)\cos(\phi_{Pg}), \tag{36a}$$

$$\eta_g = (\omega/\beta_r)\cos(\phi_{Sg}), \tag{36b}$$

$$\nu_s = (\omega/\alpha_r)\cos(\phi_{Ps}), \tag{36c}$$

$$\eta_s = (\omega/\beta_r)\cos(\phi_{Ss}). \tag{36d}$$

Since the Fourier transforms $x_g \rightarrow k_g$ and $x_s \rightarrow k_s$ decompose the data into plane wave components, it is rather easy to interpret the angles defined in Eqs. (36a)–(36d) (see Fig. 1):

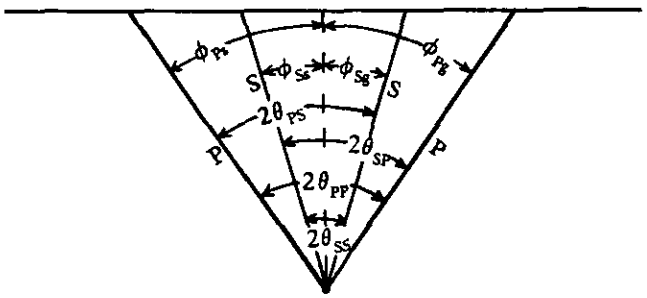

FIG. 1. Geometrical relationships of incident and reflected angles (ϕ) and half angles (θ) for compressional and shear waves (Eqs. (35a), (35b), and (37a)–(37d)).

ϕ_{Ps} is the angle between the incident compressional plane wave and the vertical;

ϕ_{Ss} is the angle between the incident shear plane wave and the vertical;

ϕ_{Pg} is the angle between the reflected compressional plane wave and the vertical;

ϕ_{Sg} is the angle between the reflected shear plane wave and the vertical.

Using these angles, another set of physically significant angles can be defined as

$$\theta_{PP} = (\phi_{Pg} + \phi_{Ps})/2, \tag{37a}$$

$$\theta_{SP} = (\phi_{Pg} + \phi_{Ss})/2, \tag{37b}$$

$$\theta_{PS} = (\phi_{Ps} + \phi_{Sg})/2, \tag{37c}$$

$$\theta_{SS} = (\phi_{Ss} + \phi_{Sg})/2. \tag{37d}$$

These angles represent the half-angles between the incident and reflected waves (Fig. 1). If the reflection is from a flat interface, θ_{PP} is the angle of incidence (and reflection) to that interface for a compressional wave, and θ_{SS} is the angle of incidence (and reflection) to that interface for a shear wave. For the converted modes, θ_{PS} and θ_{SP} are averages of the incident and reflected angles.

With the angles defined in Eqs. (37a)–(37d), the coefficients in Eqs. (25)–(28) become

$$\nu_g\nu_s - k_g k_s = (\omega/\alpha_r)^2\cos(2\theta_{PP}), \tag{38a}$$

$$k_g\nu_s + \nu_g k_s = (\omega/\alpha_r)^2\sin(2\theta_{PP}), \tag{38b}$$

$$\eta_g k_s + k_g\nu_s = (\omega^2/\alpha_r\beta_r)\sin(2\theta_{PS}), \tag{38c}$$

$$\eta_g\nu_s - k_g k_s = (\omega^2/\alpha_r\beta_r)\cos(2\theta_{PS}), \tag{38d}$$

$$\nu_g k_s + k_g\eta_s = (\omega^2/\alpha_r\beta_r)\sin(2\theta_{SP}), \tag{38e}$$

$$\nu_g\eta_s - k_g k_s = (\omega^2/\alpha_r\beta_r)\cos(2\theta_{SP}), \tag{38f}$$

$$\eta_g\eta_s - k_g k_s = (\omega/\beta_r)^2 \cos(2\theta_{SS}), \tag{38g}$$

$$k_g\eta_s + \eta_g k_s = (\omega/\beta_r)^2 \sin(2\theta_{SS}). \tag{38h}$$

Therefore, using Eqs. (35a), (35b), (36a)–(36d), and (38a)–(38h), Eqs. (25)–(28) can be written as

$$\begin{aligned} D_{PP}(k_g, k_s, \omega) = &\{1/(4\cos(\phi_{P_g})\cos(\phi_{P_s}))\} \\ &\times [\cos(2\theta_{PP})\overline{a_1}(k_g - k_s, \nu_g + \nu_s) \\ &+ \overline{a_2}(k_g - k_s, \nu_g + \nu_s) - 2(\beta_r \sin(2\theta_{PP})/\alpha_r)^2 \\ &\times \overline{a_3}(k_g - k_s, \nu_g + \nu_s)]S(\omega), \end{aligned} \tag{39}$$

$$\begin{aligned} D_{PS}(k_g, k_s, \omega) = &\{-\beta_r^2 \sin(2\theta_{PS})/(4\alpha_r^2 \cos(\phi_{S_g})\cos(\phi_{P_s}))\} \\ &\times [\overline{a_1}(k_g - k_s, \eta_g + \nu_s) + (2\beta_r \cos(2\theta_{PS})/\alpha_r) \\ &\times \overline{a_3}(k_g - k_s, \eta_g + \nu_s)]S(\omega), \end{aligned} \tag{40}$$

$$\begin{aligned} D_{SP}(k_g, k_s, \omega) = &\{\alpha_r^2 \sin(2\theta_{SP})/(4\beta_r^2 \cos(\phi_{P_g})\cos(\phi_{S_s}))\} \\ &\times [\overline{a_1}(k_g - k_s, \nu_g + \eta_s) + (2\beta_r \cos(2\theta_{SP})/\alpha_r) \\ &\times \overline{a_3}(k_g - k_s, \nu_g + \eta_s)]S(\omega), \end{aligned} \tag{41}$$

$$\begin{aligned} D_{SS}(k_g, k_s, \omega) = &\{1/(4\cos(\phi_{S_g})\cos(\phi_{S_s}))\} \\ &\times [\cos((2\theta_{SS})\overline{a_1}(k_g - k_s, \eta_g + \eta_s) \\ &+ \cos(4\theta_{SS})\overline{a_3}(k_g - k_s, \eta_g + \eta_s)]S(\omega). \end{aligned} \tag{42}$$

Thus, the triple Fourier transforms of the scattered elastic wave data are linear combinations of the double Fourier transforms of the relative changes in the medium properties expressed through a_1, a_2, and a_3. As previously mentioned, in the limit of small a_1, a_2, and a_3, these three perturbation parameters can be expressed by Eq. (24), and in this limit, Eqs. (20)–(23), and (39)–(42) become exact. The converted-reflected-wave (P-S) reflection amplitude increases with the sine of the angle between the converted wave and the incident P-wave (Eq. (40)), whereas the contribution from the shear modulus to the P-P wave changes as the square of the sine of the corresponding angle (Eq. (39)). Consequently, converted-transmitted-wave amplitudes will become significant at smaller angles than shear modulus contributions to the P-P wave.

The integrated, angular-dependent reflection coefficients $R(\mathbf{x}, \theta)$ for each of the scattering modes can now be easily extracted from Eqs. (39)–(42),

$$\begin{aligned} R_{PP}(\mathbf{x}, \theta) = &\cos(2\theta_{PP})a_1(\mathbf{x}) + a_2(\mathbf{x}) \\ &- 2(\beta_r/\alpha_r)^2 \sin^2(2\theta_{PP})a_3(\mathbf{x}), \end{aligned} \tag{43}$$

$$\begin{aligned} R_{PS}(\mathbf{x}, \theta) = &(\beta_r/\alpha_r)^2 \sin(2\theta_{PS})a_1(\mathbf{x}) \\ &+ (\beta_r/\alpha_r)^3 \sin(4\theta_{PS})a_3(\mathbf{x}), \end{aligned} \tag{44}$$

$$\begin{aligned} R_{SP}(\mathbf{x}, \theta) = &(\alpha_r/\beta_r)^2 \sin(2\theta_{SP})a_1(\mathbf{x}) \\ &+ (\alpha_r/\beta_r)\sin(4\theta_{SP})a_3(\mathbf{x}), \end{aligned} \tag{45}$$

$$R_{SS}(\mathbf{x}, \theta) = \cos(2\theta_{SS})a_1(\mathbf{x}) + \cos(4\theta_{SS})a_3(\mathbf{x}), \tag{46}$$

where the angles are defined in Eqs. (37a)–(37d) (see Fig. 1), and $\mathbf{x}$ is the reflection point between the incident and reflected rays. Although not explicit in Eqs. (43)–(46), R depends upon source and receiver coordinates x_s and x_g through the angular dependence θ. The filtered P-P reflection coefficient, $R_{PP}(\mathbf{x}, \theta)$, in Eq. (43) is identical with that of Stolt and Weglein [16].

VARIABLE BACKGROUND

For a realistic earth model, the background medium parameters will vary from location to location. If the background variations are known, their effects can be removed using the following steps (see [4, 16, 17] for explicit mathematical details):

(a) Calculate the exploding background Green's operator (projects wavefronts forward in time) and the imploding background Green's operator (projects wavefronts backward in time).

(b) Downward continue the data using the divergence theorem. When downward continuing sources and receivers, the accuracy of Eqs. (20)–(23) and (39)–(42) can be maintained through large velocity changes in a layered medium by updating ρ_r, K_r, and μ_r in each layer, as well as updating ϕ_{P_s}, ϕ_{P_g}, ϕ_{S_s}, and ϕ_{S_g} with Snell's law.

(c) Image the data by summing over ω. Steps (b) and (c) are performed with an algorithm like Stolt's [15] prestack migration. However, the obliquity factors (the A_i in Eq. (30)) differ since the linearized inverse is an amplitude-preserving prestack migration which attempts to determine relative sizes of changes in bulk modulus, shear modulus, and density.

(d) Solve a set of linear equations like Eq. (30) for A_i. The relative changes in elastic parameters a_i can then be estimated by taking different linear combinations of the $R(\mathbf{x}, \theta)$ (Eqs. (43)–(46)) (or downward-continued generalizations) over the available offsets (angles) in the moveout and divergence-corrected data, and then doing a least-squares fit (or generalized inverse) to the variations in bulk modulus, shear modulus, and density. Of course, this is contingent upon high-quality data with a sufficient range of offsets (angles).

SYNTHETIC EXAMPLES

Two synthetic models will help to illustrate the use and accuracy of our inversion process, or more appropriately termed a migration-inversion process. First, a dipping model with the reflector dipping at 6° (Fig. 2a) is analyzed. Due to the dip, the reflected energy is not spread out constantly along the reflector and the angle of incidence varies laterally for the same offset. The density and velocity variations as a function of lateral position are shown in Figs. 2b and 2c, respectively. The exact reflectivity function and the solutions using our inversion

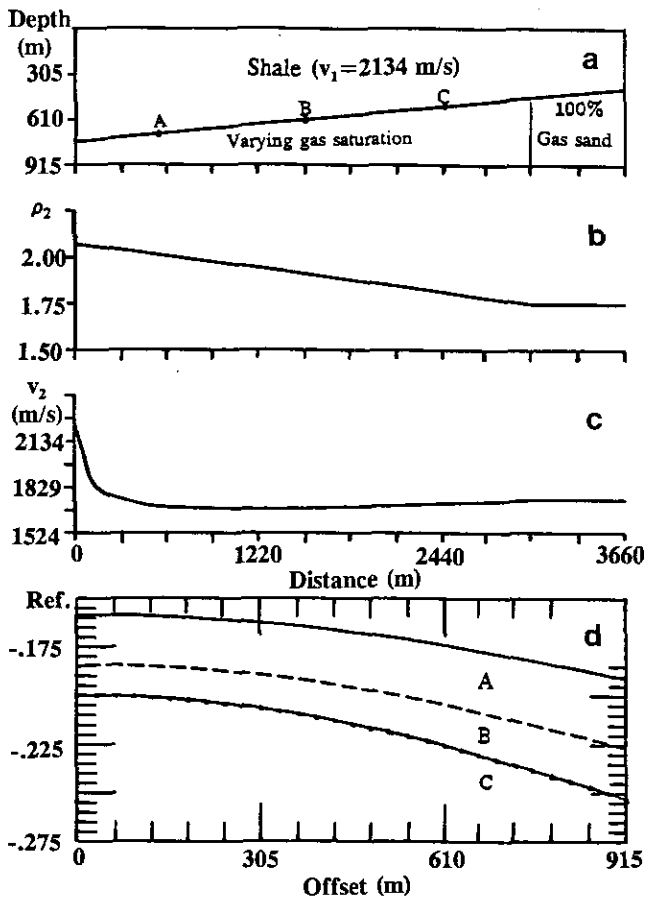

FIG. 2. Dipping model: (a) the model; (b) density variations below the reflector; (c) velocity variations below the reflector; (d) the offset-dependent reflectivities at locations A, B, and C in the model.

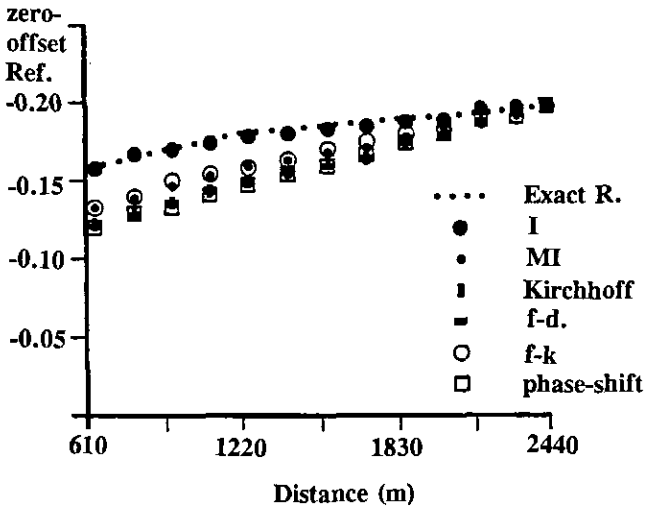

FIG. 3. Comparison of the solutions using our inversion method (I), the Stolt–Benson (1986) migration–inversion method (MI), and the Kirchhoff, finite-difference (f-d), f-k, and phase-shift migration methods for the dipping model (Fig. 2).

method, the Stolt–Benson [17] migration-inversion method, and the traditional Kirchhoff, finite-difference, *f-k*, and phase-shift migration methods are compared in Fig. 3. In order to constrain the redundant prestack data and to compensate for the actual receiver aperture, our inversion process treats the limited receiver range as a window function with respect to the ideal, full-space receiver aperture (see [17]). In addition, our method accommodates for the angle of incidence of the wave and also the dip of the reflector (see [17]). Consequently, the solution using our inversion process is much more accurate (Fig. 3) than the traditional methods. Our method preserves the amplitude information of the data very well and correctly reconstructs the zero-offset reflectivity of the reflector.

The second synthetic model is a syncline with offset-dependent reflectivities shown at locations *A*, *B*, and *C* (Fig. 4). Imaged seismograms for this model obtained using our aperture-compensated inversion process, as well as traditional Kirchhoff, finite-difference, and *f-k* methods, are shown in Fig. 5. Comparing the solutions, our inversion method is again much more accurate, although there are some small amplitude errors at the two turning points of the syncline.

Four inversions of the syncline model using our inversion scheme with several incorrect background velocities are shown in Fig. 6. The true background velocity is 3048 m/s (10,000 ft/s), but the inversions are carried out using velocities which are 10% and 20% higher and lower than this value. When the velocity error is positive, the diffraction points at the intersections of the syncline with the model edges are overcollapsed,

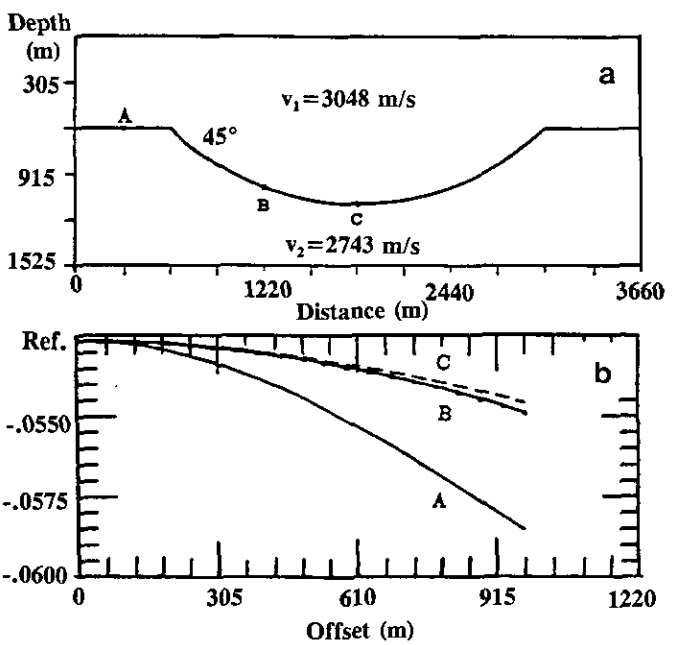

FIG. 4. Snycline model: (a) the model; (b) the offset-dependent reflectivities at locations A, B, and C in the model.

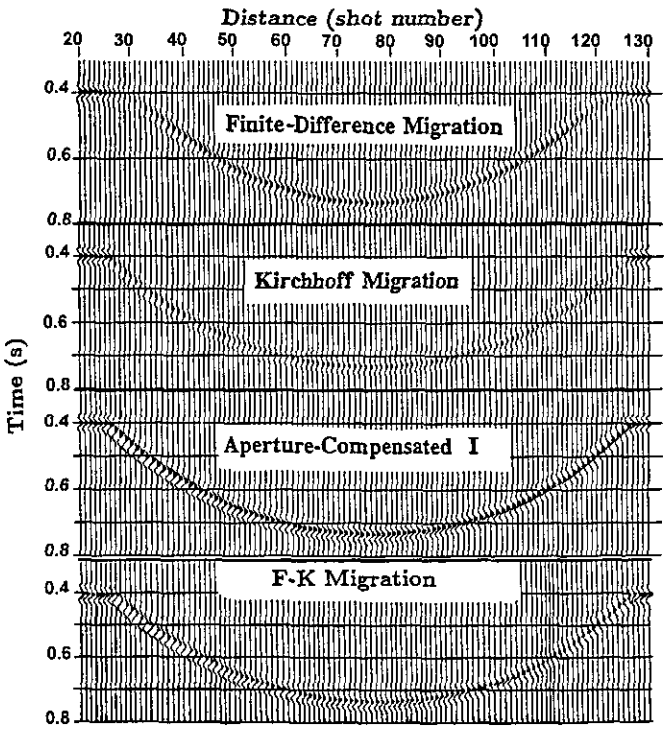

FIG. 5. Imaged seismograms for the syncline model (Fig. 4) using our inversion process (aperture-compensated I) and the Kirchhoff, finite-difference (f-d), and f-k methods.

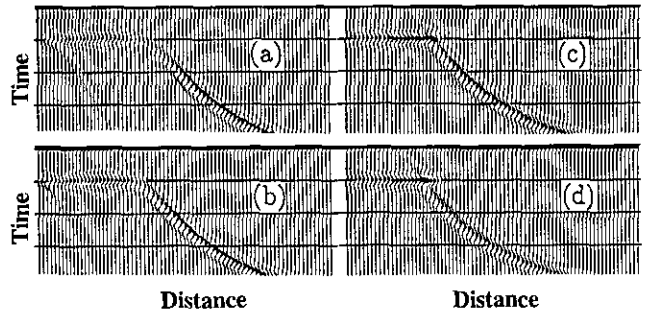

FIG. 6. Inversions of the syncline model (Fig. 4) using incorrect background velocities in our inversion process. The velocities used are (a) 2438 m/s (8000 ft/s); (b) 2743 m/s (9000 ft/s); (c) 3353 m/s (11,000 ft/s); (d) 3658 m/s (12,000 ft/s). The correct background velocity is 3048 m/s (10,000 ft/s).

and the amplitudes at these points are larger than they should be (Figs. 6c and 6d). On the other hand, when the velocity error is negative, the diffraction points are undercollapsed, and the amplitudes are smaller than they should be (Figs. 6a and 6b). From these synthetic examples and others, we conclude that if background velocity errors are within $\pm 10\%$, the inversion process is very acceptable for a continuous reflector with a moderate dip (30° or less). Furthermore, even for higher background velocity errors of $\pm 20\%$, the inversion is still acceptable if slight shifting in the reflector's location and a small error in amplitude near sharp corners of a reflector are tolerable.

REAL DATA

The above inversion algorithm was applied to a set of *P-P* data from the Gulf of Mexico, where some well control existed and water depths were approximately 300 m so that a deep tow hydrophone could monitor the source. Considerable effort was made in the acquisition and processing of the data to preserve relative amplitudes. Figures 7 through 9, respectively, show a CMP stacked section, a *f-k* prestack migrated section, and a prestack migrated/inverted section (based upon Eqs. (30)–(31d)). The latter figure shows relative changes in bulk modulus. The migrated sections (Figs. 8 and 9) show the same geological structure, but they have obvious amplitude differences since the *f-k* prestack migration did not attempt to maintain relative amplitudes, while the inversion algorithm did.

For a second example, the inversion algorithm was applied to a set of data from another area in the Gulf of Mexico where good well control existed. The data acquisition was specifically designed to gather high-quality, broadband, relative amplitude data. Experimental setup parameters, such as source and receiver spacing, choice of source, and monitoring of the source, site location, and contractor were all carefully selected in order to acquire an optimum set of data with present-day technology.

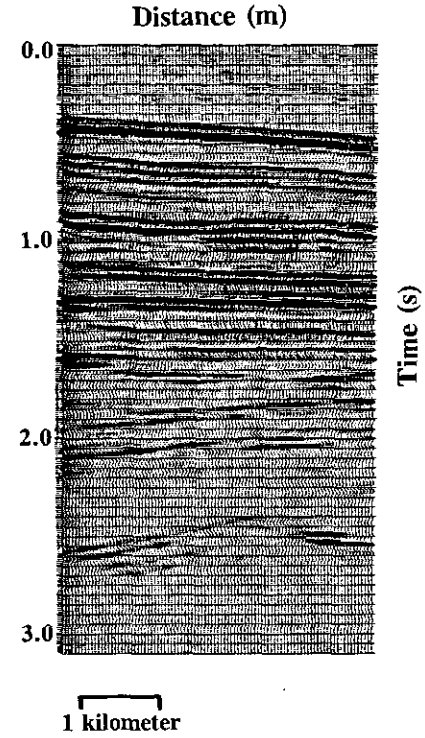

FIG. 7. CMP stacked section (P-P data) from the Gulf of Mexico (after [17]).

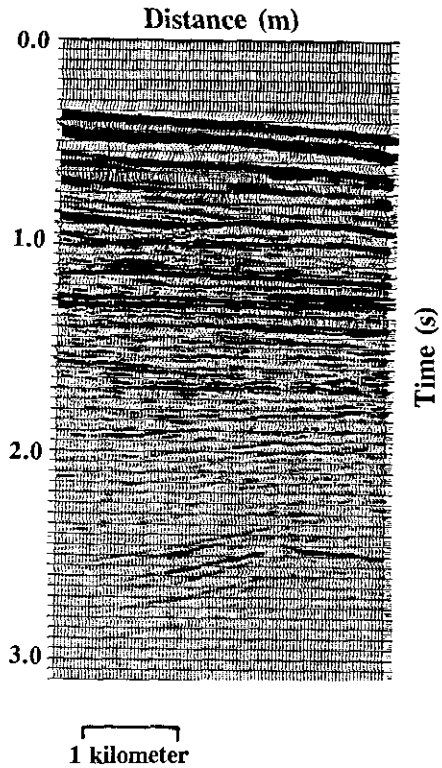

FIG. 8. F-k prestack migration of the Gulf of Mexico data used to produce Fig. 7 (after [17]).

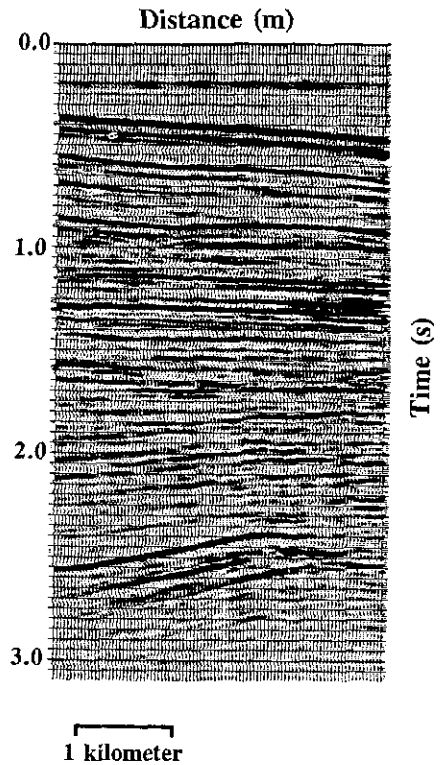

FIG. 9. Elastic wave migration/inversion of prestacked data used to produce Fig. 7. This section shows the relative changes in bulk modulus.

The specific area chosen and some of the details about the data set must remain undisclosed at present. However, as for the previous set of data, the general location in the Gulf of Mexico was where water depths are approximately 300–400 m deep so that a deep tow hydrophone could monitor the source. Part of a relative-amplitude *P-P* stacked section is shown in Fig. 10, and according to Eqs. (25)–(28) (or (39)–(42)), this section is actually a superposition of the relative changes in bulk modulus, shear modulus, and density. The amplitudes are plotted with positive amplitudes appearing dark and negative amplitudes light. Based upon Eqs. (30)–(31d), the prestack data were inverted to form the three sections shown in Figs. 11–13: (a) relative changes in bulk modulus (Fig. 11); (b) relative changes in shear modulus (Fig. 12); and (c) relative changes in density (Fig. 13).

The large negative amplitudes in bulk modulus (Fig. 11) along the horizon near 1.5 s are indicative of encountering a shale/gas sand boundary. Since, there are larger relative amplitudes at location #2 than at location #1, this indicates that the gas saturation is greater at location #2, which is in agreement with existing well log data. On the other hand, the shear modulus response (Fig. 12) along this same horizon is positive, which would be expected since sandstones are typically more rigid than unconsolidated shales in this area of the Gulf of Mexico. The larger positive response at location #1 compared to that at location #2 suggests that the sandstone near location #1 is more rigid than the sandstone near location #2, and this is again confirmed by well log data. Finally, from the relative change in density (Fig. 13), one of the largest lateral density contrasts appears between the location of lower gas saturation (#1) and the location of higher gas saturation (#2). Overall, the correlation between the inverted seismic data and the well log data obtained from wells drilled through locations #1 and #2 was

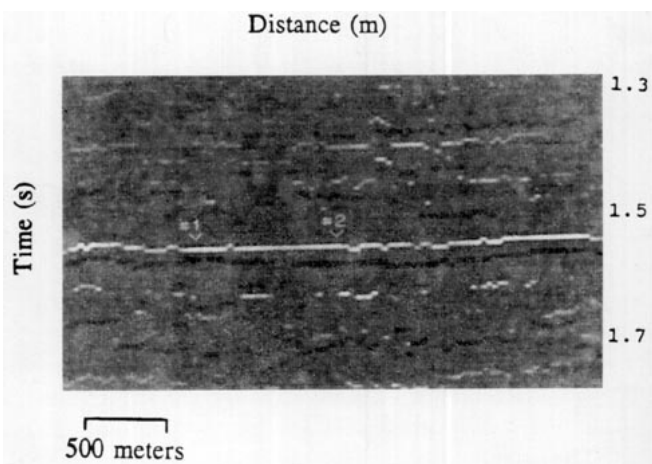

FIG. 10. Variable density display of a relative amplitude stacked section (P-P data) from the Gulf of Mexico (courtesy Conoco, Inc.).

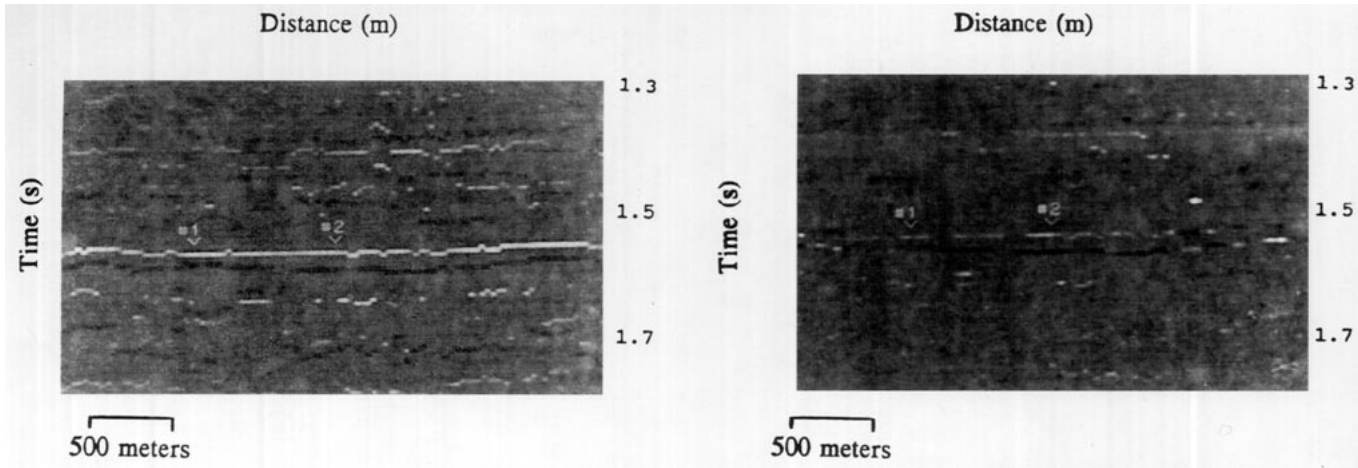

FIG. 11. Variable density display of relative changes in bulk modulus produced by elastic wave inversion of the prestacked data used in the Fig. 10 example (based upon Eqs. (30)–(31d)).

FIG. 13. Variable density display of relative changes in density produced by elastic wave inversion of the prestacked data used in the Fig. 10 example (based upon Eqs. (30)–(31d)).

very good. The well through #2 encountered a softer sandstone and a commercial gas reservoir at a depth of approximately 1560 m, whereas the well through #1 penetrated a more rigid sandstone and was noncommercial.

In summary, the relative change in bulk modulus should be a qualitative indicator of gas sands, the relative change in shear modulus should contain at least qualitative information about the "firmness" or "softness" of the reservoir rock, and the relative change in density should help delineate regions of high gas concentration [17]. However, caution must always be used in interpreting these elastic parameter changes, since magnitude and sign will depend on the particular reservoir, the surrounding rock, the depth of burial, etc. Thus, some well control in the area is necessary.

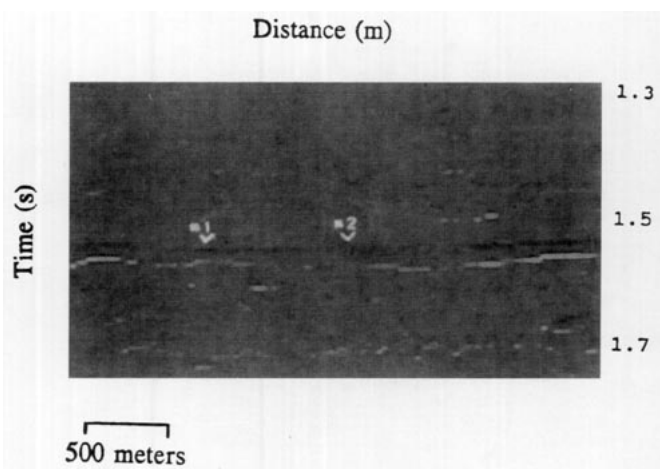

FIG. 12. Variable density display of relative changes in shear modulus produced by elastic wave inversion of the prestacked data used in the Fig. 10 example (based upon Eqs. (30)–(31d)).

CONVERTED-WAVE DATA—SOME PRACTICAL ANSWERS

The proper expressions for data recorded at the surface as pressure and shear stress are Eqs. (39)–(42). The vector com-

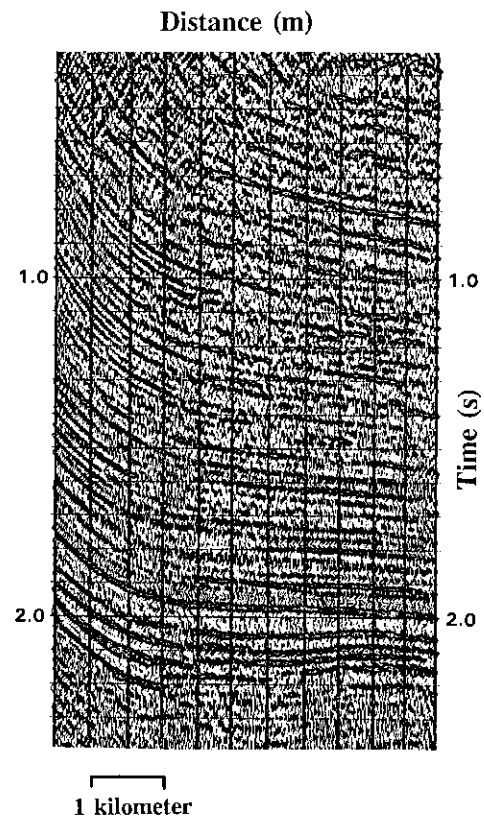

FIG. 14. P-P stacked section from southern Oklahoma (courtesy Conoco, Inc.).

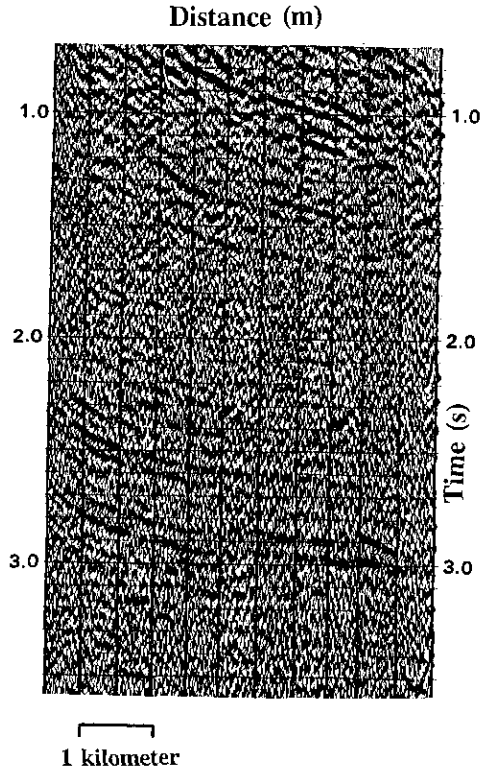

FIG. 15. P-S stacked section from southern Oklahoma (courtesy Conoco, Inc.).

prised of the components D_{PP} and D_{PS} denotes the data generated by an impulsive pressure source, while the vector formed from D_{SP} and D_{SS} is that due to an impulsive shear source. Assuming that the source is purely compressional, the relative amplitudes of D_{PS} and D_{PP} yield the relative strength of the converted waves.

From the transformation in Eq. (4),

$$\begin{pmatrix} D_{PP} \\ D_{PS} \end{pmatrix} = \begin{pmatrix} K_r & 0 \\ 0 & \mu_r \end{pmatrix} H \begin{pmatrix} U_x \\ U_z \end{pmatrix}, \tag{47}$$

where U_i are the displacement coordinates in Eq. (1). For data recorded as displacements, the inverse to Eq. (47) must be employed:

$$\begin{aligned} \begin{pmatrix} U_x \\ U_z \end{pmatrix} &= H^{-1} \begin{pmatrix} 1/K_r & 0 \\ 0 & 1/\mu_r \end{pmatrix} \begin{pmatrix} D_{PP} \\ D_{PS} \end{pmatrix} \\ &= (i/\rho_r\omega^2) \begin{pmatrix} k_g D_{PP} + \eta_g D_{PS} \\ -\nu_g D_{PP} + k_g D_{PS} \end{pmatrix}. \end{aligned} \tag{48}$$

If the direction of travel becomes vertical at the surface due to refraction, then from Eq. (35a) $k_g = 0$, and

$$U_x = (i/\rho_r\omega\beta_r)D_{PS}, \tag{49a}$$

$$U_z = (-i/\rho_r\omega\alpha_r)D_{PP}. \tag{49b}$$

For horizontal and vertical geophones of equal sensitivity, and considering a typical case of $a_2 \approx a_3$ and $\alpha \approx 2\beta$, the relative sizes of P-S and P-P reflections will be

$$\begin{aligned} r = |u_x|_{\text{typical}}/|u_z|_{\text{typical}} &\approx (\beta_r/\alpha_r)\sin(2\theta_{PS}) \\ &\approx (1/2)\sin(2\theta_{PS}). \end{aligned} \tag{50}$$

For an angle of incidence of $\approx 15°$, $\sin(2\theta_{PS}) \approx \frac{1}{2}$, and $r \approx \frac{1}{4}$. If the incident angle is $\approx 30°$ then $r \approx ((3)^{1/2}/4) \approx 0.4$. Thus, for typical reflection data, the amplitude in the horizontal channel will be about 0.25 to 0.4 of the amplitude in the vertical channel. Furthermore, if both channels have comparable noise levels, the vertical channel will have a signal-to-noise ratio

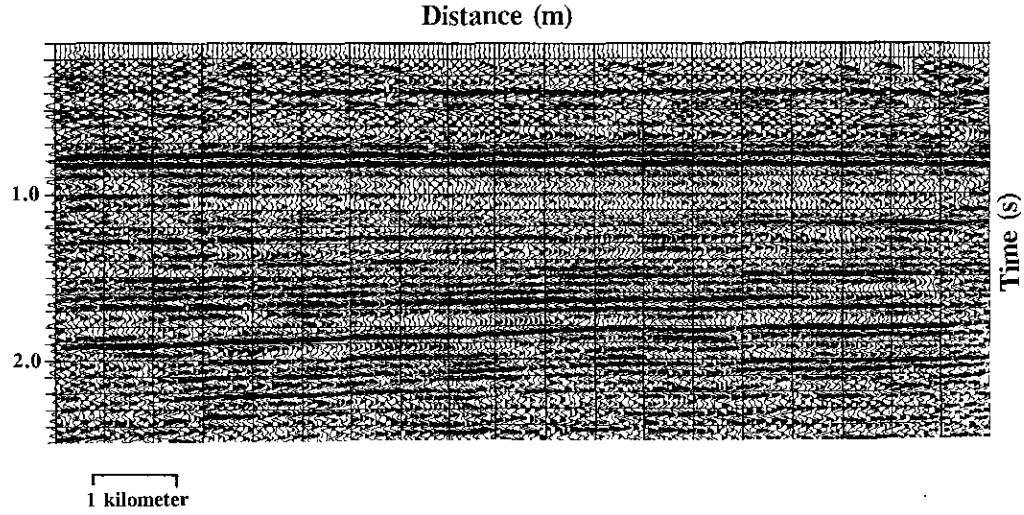

FIG. 16. P-P stacked section from western Oklahoma (courtesy Conoco, Inc.).

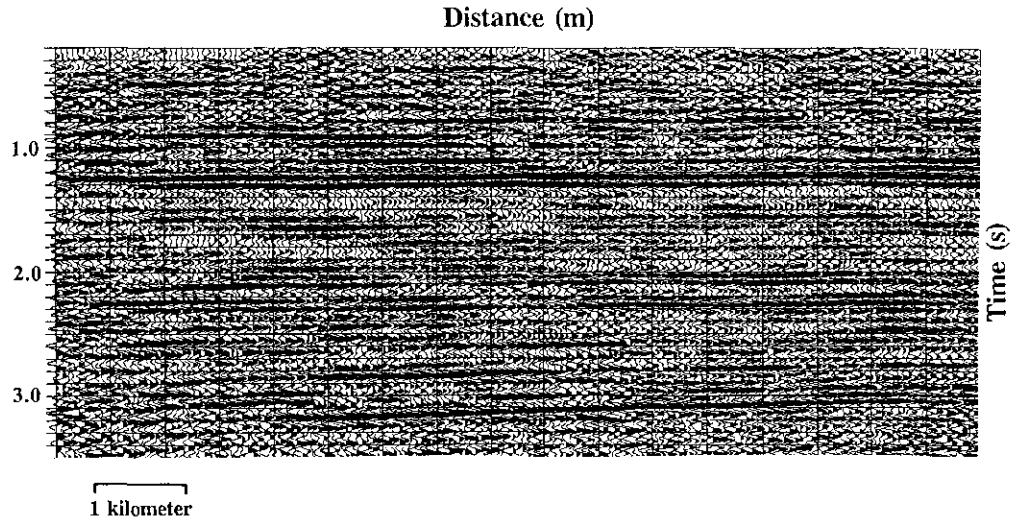

FIG. 17. P-S stacked section from western Oklahoma (courtesy Conoco, Inc.).

about 5 to 16 times greater than the horizontal channel. Due to this low SNR for the P-S waves, a significantly higher field effort will be necessary to produce a P-S section of comparable quality to the P-P section.

A P-P stacked section (Fig. 14) was produced from the vertical-array data collected by a P-wave vibrator in southern Oklahoma. The corresponding P-S stacked section constructed from the long-offset field files taken from the horizontal-array data is shown in Fig. 15. Although the SNR is marginal, some correlations can be made between the sections, and β/α ratios estimated.

Using more and longer sweeps and more geophone channels at longer offsets, P-P data and P-S data were also collected from a P-wave vibrator experiment at a site in western Oklahoma. The P-P stacked section is shown in Fig. 16 and the P-S stacked section in Fig. 17. As can be seen, the P-S section is of comparable quality to the P-P section, which is largely due to the increased field effort, but is also a function of the geology of the area. These data illustrate that significant amounts of converted (P-S) data can be generated by compressional sources. Good correlations can be made between the events in these two sections, as well as good estimates of β/α ratios.

CONCLUSIONS

Elastic wave data have been decomposed into their primary reflection components, P-P, P-S, S-P, and S-S, and the integrated, angular-dependent reflection coefficients determined for each mode by using a linearized approximation. A general prescription to invert any of these data components to recover relative variations in the medium parameters can be summarized as follows:

(1) Fourier transform the data from x_g, x_s, and t to k_g, k_s, and ω (Eq. (17));

(2) Downward continue the data to depth z with appropriate Green's operators. Update background parameters and angles (Eqs. (37a)–(37d)) in each layer. For variable background, numerically construct the WKBJ Green's operators;

(3) Image the data by summing over ω. Steps (2) and (3) would effect a prestack migration of the data;

(4) Change to a new independent variable k_z appropriate for each scattering mode (Eqs. (31a), (32a), (33a), (34a)) and form a set of linear equations like (30) for each mode, with the A's given in Eqs. (31b)–(31d), (32b)–(32d), (33b)–(33d), and (34b)–(34d). Solve for the perturbations a_i (Eqs. (13a)–(13c)) using a least-squares solution over available offsets (or available angles) in the data;

(5) Construct the angular-dependent reflection coefficients (Eqs. (43)–(46));

(6) Inverse Fourier transform over k_g-k_s and k_z to yield a spatial map of the local reflectivity as a function of the angle of incidence.

Using this algorithm for a three-parameter inversion of P-P data, the following three migrated/inverted sections would result from the input data: (1) relative changes in density, (2) relative changes in bulk modulus, and (3) relative changes in shear modulus. This was illustrated with data from the Gulf of Mexico.

Considering compressional sources, the following conclusions about reflection data recorded as displacements can be drawn from Eqs. (39)–(49):

(1) Compressional sources should generally generate significant amounts of converted (P-S) wave data.

(2) The converted (P-S) wave data (and also S-P data) respond to changes in shear modulus and density, but not to changes in bulk modulus.

(3) The P-P reflections respond to changes in all three parameters, and the shear modulus contribution to this mode is negative, which corresponds to the loss of energy due to mode conversion to P-S waves.

(4) For typical reflections, which are well within the limits of the linearized approximation, the converted (P-S) wave data is equally sensitive to increases and decreases in shear modulus.

(5) The converted-wave reflection amplitude increases with the sine of the angle between the converted wave and the incident P-wave, whereas the contribution from the shear modulus to the P-P wave increases as the square of the sine of this angle. Consequently, the converted-wave amplitudes will become significant at smaller angles than the shear modulus contribution to the P-P wave. However, as noted from Eq. (50), the signal-to-noise ratio for the converted waves will typically be smaller than that for P-P waves. This indicates that a significantly higher effort would usually be necessary to produce a good quality P-S section than needs to be made to produce a comparable P-P section, including (a) more, and probably longer, sweeps and (b) more geophone channels at longer offsets.

ACKNOWLEDGMENTS

The author extends appreciation to R. H. Stolt, A. B. Weglein, and R. W. Clayton for informative discussions and insights. Appreciation is also extended to Yongqiang Liu for typing the text.

REFERENCES

1. T. Bishop, K. Bube, R. Cutler, R. Langan, P. Love, J. Resnick, R. Shuey, D. Spindler, and H. Wyld, *Geophysics* **50,** 903 (1985).
2. N. Bleistein and S. Gray, *Geophys. Prospect.* **33,** 999 (1985).
3. P. Carrion and D. Foster, *Geophysics* **50,** 759 (1985).
4. R. Clayton and R. Stolt, *Geophysics* **46,** 1559 (1981).
5. K. Dines and R. Lytle, *Proc. IEEE* **67,** 1065 (1979).
6. W. M. Ewing, W. S. Jardetzky, and F. Press, *Elastic Wave in Layered Media* (McGraw–Hill, New York, 1957).
7. S. Ivansson, *Geophysics* **50,** 969 (1985).
8. S. Johnson and M. L. Tracy, *Ultrasonic Imaging* **5,** 361 (1983).
9. J. Justice, A. Vassiliou, S. Singh, J. Logel, P. Hansen, B. Hall, P. Hutt, and J. Solankil, *Leading Edge* **8,** 12 (1989).
10. R. Keys and A. Weglein, *J. Math. Phys.* **24,** 1444 (1983).
11. L. Lines, Inversion of geophysical data: Soc. Exploration Geophys., Tulsa, Reprint Series No. 9, 1988.
12. T. Lo, N. Toksöz, X. Shao-hui, and R. Wu, **53,** 947 (1988).
13. Y. Luo and G. T. Schuster, *Geophysics* **56,** 645 (1991).
14. B. Paulsson, N. Cook, and T. McEvilly, *Geophysics* **50,** 551 (1985).
15. R. H. Stolt, *Geophysics* **43,** 23 (1978).
16. R. H. Stolt and A. B. Weglein, *Geophysics* **50,** 2458 (1985).
17. R. H. Stolt and A. K. Benson, *Seismic Migration: Theory and Practice* (Geophysical Press, Amsterdam, 1986).
18. A. Tarantola, *Inverse Problem Theory* (Elsevier Sci., Amsterdam/New York, 1987).
19. J. R. Taylor, *Scattering Theory* (Wiley, New York, 1972).
20. N. Wattrus, "Inversion of Ground Roll Dispersion for Near-Surface Shear-Wave Velocity Variations, in *The 59th Annu. Int. Mtg., Soc. Expl. Geophys., Expanded Abstracts, 1989,* p. 946.
21. A. Weglein, 1982, *Geoexploration* **20,** 47 (1982).
22. F. Wentzel and D. Menges, *Geophysics* **54,** 1006 (1989).